

CHORUS

This is the accepted manuscript made available via CHORUS. The article has been published as:

Unveiling dislocation characteristics in Ni₃Al from stacking fault energy and ideal strength: A first-principles study via pure alias shear deformation

Shun-Li Shang, John Shimanek, Shipin Qin, Yi Wang, Allison M. Beese, and Zi-Kui Liu

Phys. Rev. B **101**, 024102 — Published 8 January 2020

DOI: [10.1103/PhysRevB.101.024102](https://doi.org/10.1103/PhysRevB.101.024102)

Unveiling dislocation characteristics in Ni₃Al from stacking fault energy and ideal strength: A first-principles study via pure alias shear deformation

Shun-Li Shang,* John Shimanek, Shipin Qin, Yi Wang, Allison M. Beese, and Zi-Kui Liu

*Department of Materials Science and Engineering, The Pennsylvania State University,
University Park, PA 16802, USA*

Abstract:

Nickel aluminide (Ni₃Al) is an important material for a number of applications, especially when used as a strengthening constituent in high-temperature Ni-based superalloys. Despite this, there is minimal information on its mechanical properties such as strength, plasticity, creep, fatigue, and fracture. In the present work, a first-principles based pure alias shear deformation has been applied to shed light on dislocation characteristics in Ni₃Al using the predicted stacking fault energy (i.e., the γ -surface) and ideal shear strength (τ_{IS}). Results include direct evidence for the splitting of a $1/2[\bar{1}10]$ dislocation into two Shockley partials on the $\{111\}$ plane, which is further supported by the equivalence of the complex stacking fault (CSF) energy γ_{CSF} and the antiphase boundary (APB) energy γ_{APB111} . Estimates of the Peierls stresses using τ_{IS} and elastic properties suggest the prevalence of edge dislocations in Ni and screw dislocations in Ni₃Al, agreeing with experimental observations regarding the dominance of edge dislocations in the first stage of crystal deformation in fcc metals and the yield strength anomaly related to screw dislocations in Ni₃Al. The present calculations further point out that the CSF and APB111 are easily formed by shear due to the low energy barriers, [although the lowest](#) planar energies are for the superlattice intrinsic stacking fault (SISF) and the APB001. Through the case of Ni₃Al, the

* Corresponding author. E-mail address: sus26@psu.edu

present work demonstrates that the pure alias shear methodology is not only computationally efficient but also provides valuable insight into the nature of shear-related properties.

1. Introduction

Shear deformation and associated properties such as stacking fault energy, γ , ideal (or theoretical) shear strength, τ_{IS} , and critical resolved shear stress (CRSS), τ_{CRSS} , are fundamental for understanding and modeling a vast number of materials properties and phenomena related to dislocations, plastic deformation, crystal growth, and phase transitions [1,2]. One example is the rise of yield strength with temperature, known as a yield strength anomaly (YSA), that occurs in the presently studied Ni_3Al and other materials with the $L1_2$ structure [3,4]. It is generally agreed that the YSA occurs primarily due to thermally activated cross-slip of screw dislocations from the $\{111\}$ primary glide plane to the $\{001\}$ cross-slip plane [5,6], where they remain locked in Kear-Wilford (KW) configurations [7]. The occurrence of the YSA can be understood using energies in the γ -surface of Ni_3Al – i.e., the energetic landscape of the generalized stacking fault energy [1] – including the antiphase boundary energy (γ_{APB111}), the complex stacking fault energy (γ_{CSF}), and the superlattice intrinsic stacking fault energy (γ_{SISF}) on the $\{111\}$ slip plane, as well as the γ_{APB001} on the $\{001\}$ cross-slip plane [3]. It is believed that the R value,

$$R = \gamma_{APB111}/\gamma_{APB001} \quad \text{Eq. 1}$$

determines the driving force of cross-slip to form KW locks [8], and the condition $R > \sqrt{3}$ indicates favorability of the KW locks according to the Paidar-Pope-Vitek model [9]. In addition to the value of γ_{APB} , a low value of γ_{CSF} reduces thermal activation necessary for the formation of KW locks [3]. Besides providing an understanding for the YSA, energies in the γ -surface can also be used to predict solid-solution strengthening and thermal cross-slip stress as shown for Mg alloys [10,11]; to explore twinnability as demonstrated for fcc and hcp metals [1,12]; and to study dislocation nucleation at a crack tip via the value of $\sqrt{\gamma_{US}}$ (where γ_{US} is the unstable stacking fault energy) according to the Rice criterion [13].

The ideal shear strength τ_{IS} is also fundamental to material behavior [1]. The value of τ_{IS} sets an upper bound on the attainable stress [14] related to such topics as (i) the minimum stress needed to plastically deform a perfect single crystal, (ii) the formation of a stacking fault, and (iii) materials strength and the extent of dislocation cores in a particular material [1,15]. Notably, τ_{IS} is a key parameter to estimate the Peierls stress – the force required to move an individual dislocation. The Peierls stress, τ_P , is approximately equal to τ_{CRSS} at 0 K [16]. For the case of a wide dislocation and according to Joós and Duesbery [17],

$$\tau_P = \frac{Kb}{a} \exp(-2\pi\zeta/a) \quad \text{Eq. 2}$$

where b is the Burgers vector, a the row spacing of atoms within the slip plane, K an elastic factor, and ζ the half-width of the dislocation with $\zeta = \frac{Kb}{4\pi\tau_{IS}}$. For an isotropic crystal, $K_{iso} = \mu(\frac{\sin^2\theta}{1-\nu} + \cos^2\theta)$ with μ being shear modulus, ν being Poisson's ratio, and θ the angle between the dislocation line and its Burgers vector with 0° for screw dislocations and 90° for edge dislocations. The Peierls stress, τ_P , is hence essentially proportional to τ_{IS} based on Eq. 2. Furthermore, these stresses (τ_{IS} , τ_P , and/or τ_{CRSS}) are key inputs for continuum models such as finite-element and phase-field simulations to predict plastic deformation and recrystallization [18,19].

Determining stacking fault energy, γ , and ideal shear strength, τ_{IS} , from experiments is not a trivial task. Weak-beam transmission electron microscopy (TEM) images can be used to calculate γ values [3], and τ_{IS} values may be determined from well-controlled nanoindentation tests [20]. Relevant to the present Ni_3Al system, the measured γ values using weak-beam TEM

by Karnthaler et al. [3] are widely accepted (see the values in Table 1). Karnthaler et al. [3] showed that the value of $\gamma_{\text{APB}_{111}}$ (175 ± 15 mJ/m²) is in general lower than that of γ_{CSF} (235 ± 40 mJ/m²). Based on the relationship between the γ values and the splitting of dislocations in fcc metals (e.g., Al, Cu, and Ni [15,21]), the inequivalent values of $\gamma_{\text{APB}_{111}}$ and γ_{CSF} by Karnthaler et al. [3] make it difficult to understand the splitting of $1/2[\bar{1}10]$ dislocation into two Shockley partials on the $\{111\}$ plane [22],

$$\frac{1}{2}[\bar{1}10] \rightarrow \frac{1}{6}[\bar{2}11] + \text{CSF} + \frac{1}{6}[\bar{1}2\bar{1}] \quad \text{Eq. 3}$$

Note that direct observations of dislocation core splitting from first-principles based calculations can be made through the present pure alias shear deformation methodology as shown in Al and Cu [21], Ni [15], and Ni₃Al (this work). Additionally, core splitting can be observed using the lattice Green's function approach to explore equilibrium dislocation geometries and associated strength and ductility as demonstrated in Al [23,24], Fe [25], W [26], and Mg-Y alloy [27].

Regarding the ideal shear strength, τ_{IS} , it is generally believed that the τ_{IS} value of Ni₃Al (around 8 GPa) is roughly equal to that of Ni according to nanoindentation experiments [28]. This τ_{IS} value is in good agreement with the commonly-accepted approximation that τ_{IS} is on the order of $\mu/10$ (shear modulus $\mu = 76$ GPa for Ni₃Al based on the measured elastic constants [29] and the Hill approach [30]). However, the predicted Peierls stress τ_{P} of Ni₃Al using $\tau_{\text{IS}} = 8$ GPa and Eq. 2 is at least one order of magnitude higher than experimental τ_{CRSS} values (see details in Sec. 3.2).

Unlike large uncertainties in estimating γ and τ_{IS} values from experiments, theoretical calculations are expected to simulate accurately shear deformation and associated properties.

Existing calculations in Ni₃Al usually use the slab model (with vacuum) to estimate planar fault energies [31] and the non-pure shear deformation for stress [32]. The slab model results in smooth yet less insightful strain versus energy (or stress) curves [31,32] due to the deformation of atoms instead of lattice vectors during shear. This makes full relaxations (except for the one fixed angle required in pure shear deformation) difficult; see details about relaxations below. Predicted γ and τ_{IS} values from a slab model with insufficient relaxations (for example, $\gamma_{CSF} = 205 \text{ mJ/m}^2$ and $\gamma_{APB111} = 180 \text{ mJ/m}^2$ [33], and $\tau_{IS} = 5.8 \text{ GPa}$ for $\{111\}\langle 110\rangle$ shear [32]; see details in Table 1) hence cannot provide more valuable insight into dislocation characteristics of Ni₃Al than the aforementioned experimental values.

It is worth mentioning that first-principles calculations based on density functional theory (DFT) are usually performed at 0 K, but the predicted results are comparable to experimental data measured at room temperature (298 K) for many properties. For example, DFT calculations of enthalpy of formation (ΔH) for metal sulfides indicate that the difference of ΔH is negligible ($< 0.2 \text{ kJ/mol}$) between 0 K and room temperature [34]. Additionally, DFT calculations using the quasiharmonic approach show that the predicted bulk moduli of Ni and Ni₃Al decrease about 9 GPa (5 %) from 0 K to room temperature [35], and the DFT based quasistatic approach indicates that ideal shear strength of Ni decreases about 0.1 GPa (only 2 %) [15]. Furthermore, Eq. 2 shows that Peierls stress, τ_p , increases with increasing ideal shear strength, τ_{IS} , but decreases with increasing elastic properties, implying the net change of τ_p value from 0 K to room temperature will be smaller than either individual effect. In the present work, all DFT calculations were performed at 0 K while all experimental data were gathered at room temperature.

Considering the significance of shear deformation and associated properties in Ni₃Al and the lack of detailed insights available in the literature, the present work aims to perform first-principles calculations of pure alias shear deformation, using the underlying science to unveil the relationship among stacking fault energy, ideal shear strength, and dislocation characteristics in Ni₃Al. Unlike partial relaxations of the supercell used widely in the literature (such as in the slab model [31]), here, the pure shear deformation indicates that all relaxations, including cell shape, cell volume, and atomic positions, are allowed except for the fixed shear angle. Furthermore, in alias shear, only one atomic plane is involved in shear deformation while the other atoms initially remain in their original positions. The displacement then propagates through the supercell due to the interaction between the atoms during the shear processes [1,15,21]; see the schematic in Figure 1 for the case of $n = 1$. In comparison to affine shear (where $n = \infty$ in Figure 1), pure alias shear represents a deformation closer to actual shear processes [21], and generates both the γ -surface and the ideal shear [strength](#).

More insights can hence be gained, as shown in the present study of Ni₃Al where findings include (i) the direct observation of dislocation decomposition according to Eq. 3; (ii) the equivalent γ_{APB111} and γ_{CSF} ; and (iii) the prevalence of screw dislocations in Ni₃Al based on the predicted τ_p using Eq. 2.

2. Methodology

2.1. Alias shear deformation of Ni₃Al

As schematically shown in Figure 1, the alias shear with one sliding layer ($n = 1$), which is closer to the actual shear situations, was adopted in the present work to study Ni₃Al with L1₂ structure.

By considering the dominant slip systems of $\{001\}\langle 110\rangle$ and $\{111\}\langle 110\rangle$ in Ni_3Al [36] as well as the splitting of $1/2[\bar{1}10]$ dislocation shown in Eq. 3, two supercells were built for the facility of first-principles calculations, namely, (i) a 16-atom tetragonal supercell with lattice vectors \mathbf{a}_{tet} , \mathbf{b}_{tet} , and \mathbf{c}_{tet} of respective lengths $\sqrt{2}a_0$, $\sqrt{2}a_0$, and $2a_0$ (where a_0 is the lattice parameter of the L_{12} lattice) parallel to the $[1\bar{1}0]$, $[110]$, and $[001]$ directions of the conventional L_{12} lattice; and (ii) a 24-atom orthorhombic supercell with lattice vectors \mathbf{a}_{orth} , \mathbf{b}_{orth} , and \mathbf{c}_{orth} of respective lengths $\sqrt{6}a_0$, $\sqrt{2}a_0$, and $\sqrt{3}a_0$ parallel to the $[11\bar{2}]$, $[\bar{1}10]$, and $[111]$ directions; see the orthorhombic supercell in Figure 1. It is worth mentioning that the alias shear deformation of $\{001\}\langle 110\rangle$ generates the APB001 fault; the alias shear deformation of $\{111\}\langle 11\bar{2}\rangle$ along the easy and hard directions generates the planar faults of CSF and SISF, respectively [14]; and the alias shear deformation of $\{111\}\langle \bar{1}10\rangle$ generates the APB111 fault.

After alias shear of the tetragonal or the orthorhombic supercell, the deformed lattice vector matrix $\bar{\mathbf{R}}$ can be expressed by [1,15],

$$\bar{\mathbf{R}} = \mathbf{R}\mathbf{D} \quad \text{Eq. 4}$$

where \mathbf{R} is the undeformed lattice vector matrix, and \mathbf{D} the deformation matrix. For example, the \mathbf{D} matrices for the $\{111\}\langle 11\bar{2}\rangle$ and $\{111\}\langle \bar{1}10\rangle$ shears of the aforementioned orthorhombic supercell are as follows,

$$\mathbf{D}_{\langle 11\bar{2}\rangle} = \begin{bmatrix} 1 & 0 & 0 \\ 0 & 1 & 0 \\ \varepsilon & 0 & 1 \end{bmatrix} \text{ and } \mathbf{D}_{\langle \bar{1}10\rangle} = \begin{bmatrix} 1 & 0 & 0 \\ 0 & 1 & 0 \\ 0 & \varepsilon & 1 \end{bmatrix} \quad \text{Eq. 5}$$

where ε is the shear magnitude corresponding to the engineering shear strain, i.e., the ratio of shear displacement with respect to the height of the supercell [1,15]. In the present practice of first-principles calculations, Cartesian coordinates for the initial atomic positions were employed

for the facility of alias shear deformation [1,15,21]. Pure shear deformations, including relaxations of atomic positions, cell shape, and cell volume except for the fixed shear angle, were performed by an external Python optimizer GADGET developed by Bučko *et al.* [37] to control first-principles calculations of both stresses and forces acting on each atom. Note that the alias shear deformation employs only half atoms (and no vacuum layers) in the supercell in contrast to the slab model, making alias shear more computationally efficient to study shear-related properties.

2.2. First-principles calculations

All first-principles calculations in the present work were performed by the Vienna *Ab initio* Simulation Package (VASP) [38] together with the ion-electron interaction described by the projector augmented wave (PAW) method [39]. The exchange-correction functional was depicted by the generalized gradient approximation (GGA) [40], the same potential as our previous first-principles calculations for Ni-based alloys [2,15,41]. The core configurations recommended by VASP were adopted in the present work, i.e., [Ne] for Al and [Ar] for Ni. During VASP calculations, the k -point meshes of $4 \times 7 \times 6$ were used for the 24-atom orthorhombic supercell (or $8 \times 8 \times 6$ for the 16-atom tetragonal supercell) and a cutoff energy of 270 eV was employed for the plane-wave basis set according to our trial calculations. The energy convergence criterion of electronic self-consistency was selected as 10^{-5} eV per supercell for all calculations. The reciprocal-space energy integration was performed by the Methfessel-Paxton [42] technique with a 0.2 eV smearing width, which results in accurate total energies as well as stresses. Concerning pure shear deformation, [all relaxed stress components except for the one corresponding to](#) the fixed shear angle were less than 0.15 GPa, and the forces acting on

atoms were less than 0.03 eV/Å. Besides the present focus of pure alias shear, two more ancillary shear deformations were also employed for comparison: the simple alias shear without relaxations of the supercell (represented by “simple” for short) and the simple alias shear with relaxations of atomic positions only (represented by “simple+RX” for short). In addition, spin polarization was considered in all DFT calculations due to the magnetic nature of Ni.

3. Results and discussion

3.1. Shear-related properties in Ni₃Al

Figure 2 and Figure 3 illustrate the variations of planar fault energy γ , shear stress τ , and spin magnetic moment of Ni₃Al during the alias shear deformations of $\{111\}\langle 11\bar{2}\rangle$, $\{111\}\langle \bar{1}10\rangle$, and $\{001\}\langle 110\rangle$. These two figures show that only the simple shear gives smooth energy and stress curves while the relaxations (pure shear or simple+RX) lead to sudden changes of energy around the unstable shear positions, corresponding to the zero stress and the unstable stacking fault energy (γ_{US}). Furthermore, the maximum stress gives the ideal shear strength τ_{IS} and the local minimum in energy curve gives the stable stacking fault energy (γ_S). The present γ_S , γ_{US} , and τ_{IS} values as well as the corresponding engineering strains shown in Figure 2 and Figure 3 are also listed in Table 1. In general, the present predictions are in good agreement with experimental estimations [3,28,43–46] and other DFT and embedded-atom method (EAM) calculations [5,22,31–33,46,47]; see details in Table 1. For example, the present γ_{CSF} values (203 mJ/m² from pure shear and even 212 and 252 mJ/m² from simple shears) agree well with the previous calculations (120 ~ 225 mJ/m²) [5,22,31,46] and experiments (206 ~ 235 mJ/m²) [3] with large uncertainties. Among the γ_S and γ_{US} values related to CSF, SISF, APB111, and APB001 (*cf.*, Table 1), it is found that the lower γ_S values relate to the formation of SISF (72 mJ/m² from pure shear) and APB001 (64 mJ/m² from pure shear), matching reasonably well the

previous simulations ($\gamma_{\text{SISF}} = 13 \sim 80 \text{ mJ/m}^2$ and $\gamma_{\text{APB001}} = 73 \sim 121 \text{ mJ/m}^2$) and experiments ($\gamma_{\text{SISF}} = 6 \sim 276 \text{ mJ/m}^2$ and $\gamma_{\text{APB001}} = 104 \text{ mJ/m}^2$). Despite the lower γ_{SISF} and γ_{APB001} values, shear deformations to form SISF and APB001 are difficult due to the large energy barriers, e.g., $\gamma_{\text{US}} > 1000 \text{ mJ/m}^2$ based on pure shear deformation.

It is interesting to find that the stable (as well as the unstable) stacking fault energies related to the formation of CSF and APB111 from pure alias shear are almost identical, which is contrary to the experimental results by Karnthaler et al. [3], viz., $\gamma_{\text{CSF}} \approx \gamma_{\text{APB111}}$ ($203 \sim 205 \text{ mJ/m}^2$) and the γ_{US} values $\sim 230 \text{ mJ/m}^2$ for both faults (*cf.*, Table 1), providing indirect evidence about the splitting of $1/2[\bar{1}10]$ dislocation in terms of Eq. 3 (see more discussion in Sec. 3.2). The lower γ_{US} value ($\sim 230 \text{ mJ/m}^2$ to form CSF and APB111 compared to $\gamma_{\text{US}} > 1000 \text{ mJ/m}^2$ to form SISF and APB001) indicates that both CSF and APB111 are easy to be formed by shear.

The ideal shear strength τ_{IS} is in general proportional to the unstable stacking fault energy γ_{US} (see Table 1, Figure 2, and Figure 3), indicating the degree of difficulty to form a planar fault by shear in the present work. It should be mentioned that the τ_{IS} value is inversely proportional to the number of layers in the supercell [48]. [Considering the](#) limited layers (such as one layer) involved in actual shear deformation, the minimum of three $\{111\}$ layers is employed for both the tetragonal and orthorhombic supercells of the $L1_2$ lattice in the present work, corresponding to the highest τ_{IS} value to be obtained for a given shear deformation [48]. It is seen that the lowest τ_{IS} value in Ni_3Al (3.7 GPa by pure shear) is related to the formation of CSF, [followed by](#) $\tau_{\text{IS}} = 4.2 \text{ GPa}$ to form APB111. However, the τ_{IS} values are quite high ($\sim 15 \text{ GPa}$) to form SISF and APB001, agreeing with the higher γ_{US} values to form these faults. The present τ_{IS} values (3.7,

4.2, 14.8, and 15.2 GPa from different pure shear deformations) are in good agreement with the estimates from compressive strength of dislocation-free nanocube (4.15 GPa) [49], nanoindentation experiments (~ 8 and 13.5 GPa) [28,44,45], and molecular dynamic simulations (16.5 \sim 18.8 GPa) [46]; see details in Table 1. Especially the present τ_{IS} value (4.2 GPa from $\{111\}\{\bar{1}10\}$ pure shear) agrees well with the estimated resolved shear stress of 4.15 GPa according to the measured compressive strength by assuming a $\{111\}\langle 110\rangle$ slip [49]. It is worth mentioning that the lowest τ_{IS} value of Ni₃Al (3.7 GPa in the present work) is lower than that of pure Ni (5.1 GPa based on pure shear deformation [15]) due to the soft nature of Al compared to Ni (e.g., bulk moduli 74 GPa vs. 196 GPa based on DFT calculations [50]).

The degree of difficulty regarding shear deformation can be qualitatively understood via the distribution of differential charge density, $\Delta\rho$ [1,2,41,51,52]. The $\Delta\rho$ is defined as the charge density difference with respect to the reference (or non-interacting) charge density, which is determined by DFT calculations of one electronic step in the present work [1]. Based on density functional theory, the denser the $\Delta\rho$ values, the stronger the bonding between atoms. Therefore, the anisotropic $\Delta\rho$ corresponds to anisotropic properties such as elasticity in fcc Al [52], and the non-spherical distribution of $\Delta\rho$ hinders shear deformation due to the difficulty of charge redistribution, resulting in higher stacking fault energies and ideal shear strengths. As an example, Figure 4 shows the $\Delta\rho$ contour maps of Ni₃Al during the simple shear along $\{111\}\{11\bar{2}\}$. The $\Delta\rho$ around each Ni displays a cube-shaped distribution, implying the difficulty of shear deformation. During shear deformation from Figure 4a to Figure 4d, the Ni-3 atom, for instance, approaches Ni-4, resulting in the re-distribution of $\Delta\rho$ and an increasing stacking fault

energy and shear stress. The shear position in Figure 4d roughly corresponds to the maximum (unstable) stacking fault energy γ_{US} .

Furthermore, the magnetic moment of Ni_3Al is relatively small ($< 0.17 \mu_B/\text{atom}$); see Figure 2c and Figure 3c. In general, the magnetic moment of Ni_3Al decreases with increasing shear displacement and appears scattered as a function of applied strain due mainly to the sudden change of stress and energy (as well as volume, not shown here) near the regions of ideal shear strength and unstable stacking fault energy. Figure 2c and Figure 3c show that the magnetic moments of Ni_3Al are close to zero ($< 0.04 \mu_B/\text{atom}$) **in most shear positions**, especially for the cases with relaxations (pure shear and simple+RX). Note that the near-zero magnetic moment has negligible influence on the resulting total energy and stress, and hence the scattered magnetic moments are not further examined with respect to such potential factors as k -point mesh density, which was found to be significant in the cases of LaNi_5 and LaNi_5H_7 [53].

3.2. Applications of shear-related properties and dislocation characteristics in Ni_3Al

As an example, Figure 5 shows the movement of one Al atom (see Al in the original Al-1 position) on the stacking fault plane (here the number 1 after Al or Ni indicates the stacking fault plane, 2 and 3 indicate the other planes) during (a) the pure alias shear of $\{111\}\langle 11\bar{2} \rangle$ to generate the CSF (see the black \square symbols to the Ni-1 position) and (b) the pure alias shear along $\{111\}\langle \bar{1}10 \rangle$ to generate the APB111 (see the green # symbols to the Ni-3 position). It can be seen that the movement of Al during the pure alias shear of $\{111\}\langle 11\bar{2} \rangle$ is almost along the straight line from Al-1 to Ni-3. However, the movement of Al during the pure alias shear of $\{111\}\langle \bar{1}10 \rangle$ is along two $\{111\}\langle 11\bar{2} \rangle$ directions from Al-1 to Ni-2 and then to Ni-1, i.e., the

movement of Al shows directly the splitting of a $1/2[\bar{1}10]$ dislocation into two Shockley partials on the $\{111\}$ plane as indicated by Eq. 3. Note that the other atoms in the stacking fault plane show almost the same behaviors as that of Al in the Al-1 position.

To further examine the splitting of the $1/2[\bar{1}10]$ dislocation, Figure 6 shows the variations of lattice parameters and angles between them during the pure alias shear of $\{111\}\langle\bar{1}10\rangle$ in the orthorhombic supercell (see Figure 1). In the initial stage of shear up to the engineering shear strain of 0.11, the lattice parameters and angles change smoothly (see Figure 3). Around an engineering shear strain of 0.11, sudden changes in the lattice parameters occur due to reaching the ideal shear strength and unstable stacking fault energy (see Figure 3) which also coincides with a direction change in atomic movements (see Figure 5). The sudden fluctuations of lattice parameters and angles signal dislocation splitting and the appearances of γ_{US} and τ_{IS} during pure alias shear deformation.

The predicted τ_{IS} value can be used to estimate Peierls stress τ_P according to Eq. 2. In contrast to the elastic factor K_{iso} for an isotropic crystal as in Eq. 2, the elastic factor K of an anisotropic crystal is direction-dependent. For an edge dislocation aligned with the z-direction with a Burgers vector $\mathbf{b} = (b_x, b_y, 0)$, the K_{e_x} along the x-direction is given by [54],

$$K_{e_x} = (\bar{c}'_{11} + c'_{12}) \left[\frac{c'_{66}(\bar{c}'_{11} - c'_{12})}{(\bar{c}'_{11} + c'_{12} + 2c'_{66})c'_{22}} \right]^{1/2} \quad \text{Eq. 6}$$

where $\bar{c}'_{11} = (c'_{11}c'_{22})^{1/2}$, and the c'_{ij} represents the transformed elastic constants onto the slip system of interest. In the present orthorhombic supercell shown in Figure 1, for example, the transformed lattice vectors are parallel to the $[11\bar{2}]$, $[\bar{1}10]$, and $[111]$ directions. Note that for

the present Ni₃Al cell shown in Figure 1, $K_{e_x} = K_{e_y} (= K_e)$ for edge dislocations along both the x- and y-directions. In addition, the elastic factor K_s for screw dislocations of an anisotropic crystal can be expressed as [54],

$$K_s = (c'_{44}c'_{55} - c'^2_{45})^{1/2} \quad \text{Eq. 7}$$

By means of Eq. 2 (as well as Eq. 6 and Eq. 7) with input of the minimum $\tau_{IS} = 3.7$ GPa for Ni₃Al (*cf.*, Table 1) and the DFT-predicted elastic constants of Ni₃Al [55], the predicted τ_p values for both the edge (e) and screw (s) dislocation cases of Ni₃Al using both the isotropic (iso) and anisotropic (aniso) elastic factors are given in Table 2 (i.e., predictions of four cases: iso-e, iso-s, aniso-e, and aniso-s). For the sake of comparison, the predicted τ_p values of fcc Ni and the measured CRSS values at room temperatures for both Ni [56–59] and Ni₃Al [3,60,61] are also listed in Table 2 and plotted in Figure 7. All the required data to predict τ_p values of Ni₃Al and Ni are detailed as footnotes of Table 2, including τ_{IS} , c_{ij} , and lattice parameters [15,55]. Table 2 and Figure 7 show that the range of the predicted τ_p values for anisotropic crystal from edge to screw dislocations (blue symbols) is larger than that of the isotropic crystal from edge to screw dislocations (red symbols) for both Ni₃Al and Ni. It is seen that the predicted τ_p values of Ni₃Al are smaller than those of Ni due mainly to the smaller τ_{IS} used for Ni₃Al (3.7 GPa vs. 5.1 GPa for Ni₃Al and Ni, respectively; see Table 2). It can be seen that the τ_p values of Ni₃Al for screw dislocations (circular symbols) and the τ_p values of Ni for edge dislocations (square symbols), especially the values for anisotropic cases (the blue symbols), agree reasonably well with experimental CRSS values (which are scattered, see the filled grey bars as well as the values in Table 2). This comparison of calculated τ_p values and experimental CRSS values indicate the predominance of screw dislocations in Ni₃Al and edge dislocations in Ni. In terms of

experimental observations, the edge dislocation dipoles that are prevalent in stage I of fcc single crystal deformation can be explained by mutual annihilation of screw segments through cross-slip [3,62]. It was observed that Ni₃Al exhibits long and straight screw dislocations, adopting either incomplete or complete KW locking configurations, while the edge dislocations mainly act as links between the long screw dislocations and their cross-slipped parts [6,36]. It was further observed that deformation of Ni₃Al-based superalloy is dominated by screw dislocations in the early stage of tensile tests using different strain levels (from 0.8% to 8.2%) [63]. Similarly to Ni, the τ_p values of Ni₃Al from edge dislocations are lower than those from screw dislocations (see Figure 7), indicating plastic deformation should start from the easy deformed edge dislocations for both Ni and Ni₃Al. Experimentally it was observed that the mobile edge dislocations (instead of the sessile screw dislocations) contribute most to the primary creep strain in Ni₃Al [64,65]. Here, the commonly observed screw dislocations in Ni₃Al [6,36,63] may due to (i) the not enough active edge dislocations to initiate plastic deformation, (ii) the easy trigger of screw dislocations during plastic deformation, and/or (iii) the less accurate Peierls stresses predicted in the present work. Detailed dislocation mechanism in Ni₃Al can be explored using such as the crystal plasticity finite element simulations [48,63,66], but this study is beyond the scope of the present work.

The agreement between the present predictions and experimental observations on dislocation types (Table 2 and Figure 7) indicates that it is reasonable to select the minimum τ_{IS} value in Ni₃Al to predict τ_p . It is worth mentioning that the lower τ_p values in Ni₃Al can be increased by using higher τ_{IS} values. For example, from $\tau_{IS} = 3.7$ GPa (to generate the CSF) to 4.2 GPa (to generate the APB111) by considering the dominant slip system of $\{111\}\langle 110\rangle$ in Ni₃Al [36], the

predicted τ_p values increase about 2.2 to 4.5 times, and the predicted τ_p values of screw dislocations (38.6 ~ 161.8 MPa) are still in a good agreement with experimental τ_{CRSS} values (27 ~ 90 MPa); see detailed values in Table 2.

It is found that τ_{IS} is a key value to predict the half width of dislocation ζ and hence the Peierls stress, τ_p , by using Eq. 2. As an example of the use of inaccurate values, the predicted τ_p is 372 MPa for an isotropic edge dislocation using $\tau_{IS} = 8$ GPa estimated from nanoindentation [28], and the predicted τ_p is 1088 MPa for an isotropic edge dislocation using the ζ value from Poisson's ratio ν via $\zeta = \frac{d}{2(1-\nu)}$ (where d is the distance between slip planes). These τ_p values (372 and 1088 MPa) are at least one and even two orders of magnitude higher than experimental τ_{CRSS} values at room temperature (27 ~ 90 MPa; see Table 2), supporting the observations that the predicted Peierls stress is less accurate by using less accurate τ_{IS} such as the one estimated from the γ -surface [67]. It was further observed that the calculated Peierls stress can be improved by allowing strain field relaxation in the process of overcoming the Peierls potential [68].

In addition to predicting Peierls stress from τ_{IS} , the γ -surface is also fundamental to understand and model numerous material properties and phenomena as mentioned in Sec. 1. For example, the presently predicted R value (see Eq. 1) is 3.2 based on the pure alias shear deformation. As this R value is greater than $\sqrt{3}$, this indicates the possibility of forming KW locks in Ni₃Al [9]. Additionally, the D value, defined as the ratio of surface energy to unstable stacking fault energy as $D = \gamma_{surface}/\gamma_{US}$, can be used to determine the ductility by using the Rice criterion [13]. The presently predicted value of D is 16.2 using the values of $\gamma_{US} = 229$ mJ/m² to generate the CSF

(see Table 1) and $\gamma_{\text{surface}} = 3705 \text{ mJ/m}^2$ [31]; in contrast, $D = 2.8$ using the values of $\gamma_{\text{US}} = 1308 \text{ mJ/m}^2$ to generate the SISF (see Table 1). It is therefore meaningful to predict the influence of alloying elements on the R , D , and τ_{P} values of Ni_3Al or other L1_2 alloys to understand trends and design alloys. In addition, the presently employed methodology of pure alias shear provides not only a simple and accurate way to calculate shear-related properties but also gives valuable insight into dislocation characteristics.

4. Summary

The present work investigates shear-related properties with a focus on dislocation characteristics in Ni_3Al by means of a computationally efficient methodology of pure alias shear. The present first-principles results provide direct evidence concerning the splitting of the $1/2[\bar{1}10]$ dislocation into two Shockley partials on the $\{111\}$ plane (*cf.*, Eq. 3), and this splitting is further supported by the equivalent planar fault energies of γ_{CSF} and γ_{APB111} predicted by the pure alias shears on the $\{111\}$ plane. Comparing the predicted Peierls stresses τ_{P} with experimental τ_{CRSS} , the present work suggests the prevalence of screw dislocations in Ni_3Al as well as edge dislocations in Ni due to the fact that the minimum ideal shear strength of Ni_3Al is about 30% lower than that of Ni (3.7 GPa vs. 5.1 GPa).

In addition, the present dislocation characteristics agree well with experimental observations regarding (a) the dominant edge dislocations in stage I of fcc single crystal deformation; and (b) the yield strength anomaly (YSA) in Ni_3Al related to screw dislocations adopting the Kear-Wilsdorf configurations [7]. Note that the YSA also can be understood by means of empirical relationships in the literature (see the introduction) and the presently predicted planar fault

energies, ideal shear strengths, and Peierls stresses (i.e., the CRSS values at low temperatures). It is further observed that the planar faults of CSF and APB111 are easily formed by shear due to the lower energy barriers (both the lower ideal shear strength and the lower unstable stacking fault energy as shown in Table 1), although even lower planar fault energies are found for SISF and APB001. The present predictions of ideal shear strength and stacking fault energy are in favorable accord with the scattered results from experiments and other calculations. However, only the present predictions – from the pure alias shear deformation – provide more insights into the underlying science of Ni₃Al dislocation splitting and dislocation character than, for example, the commonly employed slab model. Beyond the present work, we also can explore more properties of Ni₃Al such as (i) temperature-dependent Peierls stress in Ni₃Al by means of the quasistatic approach [15]; (ii) solute strengthening in Ni₃Al by predicting the effect of alloying elements on Peierls stress (i.e., the CRSS value) using Eq. 2; and (iii) stress versus strain curve through the combination of Peierls stress and finite element simulations [48].

ACKNOWLEDGMENTS

This work was financially supported by the U. S. Department of Energy (DOE) via award no. DE-FE0031553, the Office of Naval Research (ONR) via contract no. N00014-17-1-2567, and the National Science Foundation (NSF) via grant No. CMMI-1825538. First-principles calculations were carried out partially on the ACI clusters at the Pennsylvania State University, partially on the resources of NERSC supported by the DOE Office of Science under contract no. DE-AC02-05CH11231, and partially on the resources of XSEDE supported by NSF via grant no. ACI-1548562.

Tables and Table Captions

Table 1. Calculated (Calc.) properties in Ni₃Al related to alias shear deformation in comparison with data in the literature (Expt., results at room temperature) including the stable and unstable stacking fault energies in mJ/m² (γ_s and γ_{US} , respectively), the ideal shear strength τ_{IS} in GPa, and the corresponding engineering strains ϵ (see its definition in Eq. 5).

Shear	ϵ_s	γ_s	ϵ_{US}	γ_{US}	ϵ_{IS}	τ_{IS}	Notes and references
(111)[112]	0.20	203	0.13	229	0.12	3.7	Calc., this work, pure shear
CSF	0.20	212	0.14	254	0.10	5.1	Calc., this work, simple shear, relaxed
	0.20	252	0.14	284	0.07	2.2	Calc., this work, simple shear, unrelaxed
		205 ^a		254			Calc., DFT, slab model [31]
		225					Calc., DFT [22]
		223					Calc., DFT + Peierls model [5]
		120 ~ 218					Calc., several EAM simulations [46]
		235±40					Expt., weak-beam TEM images [3]
	206±30					Expt., for alloy Ni ₇₆ Al ₂₄ [3]	
(111)[112]	0.47	72	0.23	1308	0.22	15.2	Calc., this work, pure shear
SISF	0.47	92	0.24	2273	0.14	9.4	Calc., this work, simple shear, unrelaxed
		75 ^a		1368			Calc., DFT, slab model [31]
		80					Calc., DFT [22]
		79			0.32	13.7	Calc., DFT, not pure shear [32]
		13 ~ 51					Calc., DFT + Peierls model [5]
		6±0.5					Calc., several EAM simulations [46]
		10 ~ 276					Expt., weak-beam TEM images [3]
						Expt., from several resources [43]	
(111)[110]	0.16	205	0.119	230	0.12	4.2	Calc., this work, pure shear
APB111	0.41	215	0.272	582	0.12	7.6	Calc., this work, simple shear, relaxed
	0.41	314	0.214	1080	0.10	4.8	Calc., this work, simple shear, unrelaxed
		180 ^a		778			Calc., DFT, slab model [31]
		178					Calc., DFT results at 100 K [33]
		210					Calc., DFT [22]
		172			0.18	5.8	Calc., DFT, not pure shear [32]
		142~252					Calc., DFT + Peierls model [5]
		175±15					Calc., several EAM simulations [46]
		180±20					Expt., weak-beam TEM images [3]
		206±22					Expt., for alloy Ni ₇₆ Al ₂₄ [3]
					4.15		Expt. [3]
							Expt. for dislocation-free Ni ₃ Al [49]
(001)[110]	0.37	64	0.17	1152	0.16	14.8	Calc., this work, pure shear
APB001	0.35	110	0.18	1200	0.15	14.8	Calc., this work, simple shear, relaxed
	0.35	119	0.19	2084	0.10	7.9	Calc., this work, simple shear, unrelaxed
		121					Calc., DFT + Peierls model [47]
		73					Calc., DFT results at 100 K [33]
		74~102					Calc., several EAM simulations [46]
		104±15					Calc., several EAM simulations [46]
						Expt., weak-beam TEM images [3]	
Unspecified						13.5	Expt., nanoindentation [44]
						~8	Expt., nanoindentation [28,45]
						18.8	Expt. plus Calc. (MD simulations) [46]

^a Estimated values based on the published figures [31].

Table 2. Calculated Peierls stresses (τ_p , MPa) at 0 K for four cases of edge (e) and screw (s) dislocations using elastic factors for isotropic (iso) and anisotropic (aniso) crystals in comparison with experimental CRSS values (τ_{CRSS} , MPa) at room temperature for both Ni_3Al and Ni.

Material	τ_p (iso-e)	τ_p (iso-s)	τ_p (aniso-e)	τ_p (aniso-s)	Experimental τ_{CRSS}
Ni_3Al ^a	0.7 ^b 3.0 ^c 1088 ^d	14.2 ^b 38.6 ^c 0.4 ^d	0.4 ^b 1.8 ^c	75.0 ^b 161.8 ^c	27 ± 5, ^e 75±20, ^f 40-90 ^g
Ni ^a	19.2 ^b 49.7 ^c	168.7 ^b 327.5 ^c	14.4 ^b 38.5 ^c	374.5 ^b 651.0 ^c	5.7, ^h 5.9~8.3, ⁱ 9.9, ^j 10.2, ^k 17.5 ^l

^a Elastic constants (c_{ij}) and lattice parameters a_0 to predict τ_p by Eq. 2 were taken from our previous DFT calculations, i.e., $c_{11} = 242$ GPa, $c_{12} = 152$ GPa, $c_{44} = 125$ GPa, and $a_0 = 3.57$ Å for Ni_3Al [55]; and $c_{11} = 273$ GPa, $c_{12} = 160$ GPa, $c_{44} = 114$ GPa, and $a_0 = 3.52$ for Ni [48].

^b The lowest τ_{IS} values of $\{111\}\langle 11\bar{2} \rangle$ slip were used to predict τ_p , i.e., $\tau_{IS} = 3.7$ GPa for Ni_3Al (see Table 1) and $\tau_{IS} = 5.1$ GPa for Ni [15].

^c The second lowest τ_{IS} values of $\{111\}\langle \bar{1}10 \rangle$ slips were used to predict τ_p , i.e., 4.2 GPa for Ni_3Al (see Table 1) and 5.8 GPa for Ni [15].

^d For reference only using the Poisson's ratio (estimated by c_{ij} values and the Voigt approach) to predict the half width of dislocation and then τ_p .

^e CRSS value for Ni_3Al sample with 78 at.% Ni and 22 at.% Al as well as 0.2% plastic strain [3].

^f CRSS value of tensile tests for Ni_3Al samples with 77 at.% Ni and 23 at.% Al for (111)[110] slip [60].

^g Orientation-dependent CRSS values of Ni_3Al alloys [61].

^h CRSS value of Ni measured in 1933 [56].

ⁱ CRSS value of Ni measured in 1958 [57].

^j CRSS value of Ni measured in 2016 [69].

^k CRSS value of Ni measured in 1951 [58].

^l CRSS value of Ni measured in 2005 [59].

References:

- [1] S. L. Shang, W. Y. Wang, B. C. Zhou, Y. Wang, K. A. Darling, L. J. Kecskes, S. N. Mathaudhu, and Z. K. Liu, *Acta Mater.* **67**, 168 (2014).
- [2] S. L. Shang, C. L. Zacherl, H. Z. Fang, Y. Wang, Y. Du, and Z. K. Liu, *J. Phys. Condens. Matter* **24**, 505403 (2012).
- [3] H. P. Karnthaler, E. T. Mühlbacher, and C. Rentenberger, *Acta Mater.* **44**, 547 (1996).
- [4] Y. Umakoshi, D. P. Pope, and V. Vitek, *Acta Metall.* **32**, 449 (1984).
- [5] G. Schoeck, S. Kohlhammer, and M. Fahnle, *Philos. Mag. Lett.* **79**, 849 (1999).
- [6] Y. M. Wang-Koh, *Mater. Sci. Technol.* **33**, 934 (2017).
- [7] B. H. Kear and H. G. F. Wilsdorf, *Trans. Metall. Soc. AIME* **224**, (1962).
- [8] Y. Abate, S. Gamage, Z. Li, V. Babicheva, M. H. Javani, H. Wang, S. B. Cronin, and M. I. Stockman, *Light Sci. Appl.* **5**, e16162 (2016).
- [9] V. Paidar, D. . Pope, and V. Vitek, *Acta Metall.* **32**, 435 (1984).
- [10] J. A. Yasi, L. G. Hector, and D. R. Trinkle, *Acta Mater.* **59**, 5652 (2011).
- [11] J. A. Yasi, L. G. Hector, and D. R. Trinkle, *Acta Mater.* **60**, 2350 (2012).
- [12] N. Bernstein and E. Tadmor, *Phys. Rev. B* **69**, 094116 (2004).
- [13] J. R. Rice, *J. Mech. Phys. Solids* **40**, 239 (1992).
- [14] Y.-L. Liu, Y. Zhang, H.-B. Zhou, G.-H. Lu, and M. Kohyama, *J. Phys. Condens. Matter* **20**, 335216 (2008).
- [15] S. L. Shang, W. Y. Wang, Y. Wang, Y. Du, J. X. Zhang, A. D. Patel, and Z. K. Liu, *J. Phys. Condens. Matter* **24**, 155402 (2012).
- [16] P. Cordier, J. Amodeo, and P. Carrez, *Nature* **481**, 177 (2012).
- [17] B. Joós and M. S. Duesbery, *Phys. Rev. Lett.* **78**, 266 (1997).
- [18] A. Gaubert, Y. Le Bouar, and A. Finel, *Philos. Mag.* **90**, 375 (2010).
- [19] C. Zambaldi, F. Roters, D. Raabe, and U. Glatzel, *Mater. Sci. Eng. A* **454–455**, 433 (2007).
- [20] J. Li, *MRS Bull.* **32**, 151 (2007).
- [21] M. Jahnatek, J. Hafner, M. Krajci, M. Jahnátek, J. Hafner, and M. Krajčí, *Phys. Rev. B* **79**, 224103 (2009).
- [22] O. N. Mryasov, Y. N. Gornostyrev, M. van Schilfgaarde, and A. J. Freeman, *Acta Mater.* **50**, 4545 (2002).
- [23] C. Woodward, D. R. Trinkle, L. G. Hector, and D. L. Olmsted, *Phys. Rev. Lett.* **100**, (2008).
- [24] G. P. M. Leyson, W. A. Curtin, L. G. Hector, and C. F. Woodward, *Nat. Mater.* **9**, 750 (2010).
- [25] M. R. Fellingner, A. M. Z. Tan, L. G. Hector, and D. R. Trinkle, *Phys. Rev. Mater.* **2**, (2018).
- [26] Y.-J. Hu, M. R. Fellingner, B. G. Bulter, Y. Wang, K. A. Darling, L. J. Kecskes, D. R. Trinkle, and Z.-K. Liu, *Acta Mater.* **141**, 304 (2017).
- [27] D. Buey, L. G. Hector, and M. Ghazisaeidi, *Acta Mater.* **147**, 1 (2018).
- [28] J. Pokluda, M. Černý, M. Šob, and Y. Umeno, *Prog. Mater. Sci.* **73**, 127 (2015).
- [29] J. Frankel, J. Vassiliou, J. C. Jamieson, D. P. Dandekar, and W. Scholz, *Phys. B+C* **139–140**, 198 (1986).
- [30] R. Hill, *Proc. Phys. Soc. Sect. A* **65**, 349 (1952).
- [31] X.-X. Yu and C.-Y. Wang, *Mater. Sci. Eng. A* **539**, 38 (2012).
- [32] Y.-J. Wang and C.-Y. Wang, *Scr. Mater.* **61**, 197 (2009).

- [33] V. R. Manga, S.-L. Shang, W. Y. Wang, Y. Wang, J. Liang, V. H. Crespi, and Z.-K. Liu, *Acta Mater.* **82**, 287 (2015).
- [34] S.-L. Shang, Y. Wang, T. J. Anderson, and Z.-K. Liu, *Phys. Rev. Mater.* **3**, 015401 (2019).
- [35] S.-L. Shang, Y. Wang, D. Kim, and Z.-K. Liu, *Comput. Mater. Sci.* **47**, 1040 (2010).
- [36] P. R. Bhowal and M. Metzger, *Metall. Trans. A* **9**, 1027 (1978).
- [37] T. Bučko, J. Hafner, and J. G. Ángyán, *J. Chem. Phys.* **122**, 124508 (2005).
- [38] G. Kresse and J. Furthmüller, *Phys. Rev. B* **54**, 11169 (1996).
- [39] G. Kresse and D. Joubert, *Phys. Rev. B* **59**, 1758 (1999).
- [40] J. P. Perdew, J. A. Chevary, S. H. Vosko, K. A. Jackson, M. R. Pederson, D. J. Singh, and C. Fiolhais, *Phys. Rev. B* **46**, 6671 (1992).
- [41] S. L. Shang, D. E. Kim, C. L. Zacherl, Y. Wang, Y. Du, and Z. K. Liu, *J. Appl. Phys.* **112**, 053515 (2012).
- [42] M. Methfessel and A. T. Paxton, *Phys. Rev. B* **40**, 3616 (1989).
- [43] R. E. Voskoboinikov and C. M. F. Rae, *IOP Conf. Ser. Mater. Sci. Eng.* **3**, 012009 (2009).
- [44] W. Wang, C. B. Jiang, and K. Lu, *Acta Mater.* **51**, 6169 (2003).
- [45] Y. Chiu and A. H. Ngan, *Acta Mater.* **50**, 1599 (2002).
- [46] K. Xiong, H. Lu, and J. Gu, *Comput. Mater. Sci.* **115**, 214 (2016).
- [47] S. Kohlhammer, M. Fähnle, and G. Schoeck, *Scr. Mater.* **39**, 359 (1998).
- [48] S. Qin, S.-L. Shang, J. Shimanek, Z.-K. Liu, and A. M. Beese, Unpublished work (2019).
- [49] R. Maaß, L. Meza, B. Gan, S. Tin, and J. R. Greer, *Small* **8**, 1869 (2012).
- [50] S. L. Shang, A. Saengdeejing, Z. G. Mei, D. E. Kim, H. Zhang, S. Ganeshan, Y. Wang, and Z. K. Liu, *Comput. Mater. Sci.* **48**, 813 (2010).
- [51] S. Ogata, J. Li, and S. Yip, *Science* **298**, 807 (2002).
- [52] P. N. H. Nakashima, A. E. Smith, J. Etheridge, and B. C. Muddle, *Science* **331**, 1583 (2011).
- [53] L. G. Hector, J. F. Herbst, and T. W. Capehart, *J. Alloys Compd.* **353**, 74 (2003).
- [54] J. P. Hirth and J. Lothe, *Theory of Dislocations* (Krieger Pub. Co, 1992).
- [55] D. E. Kim, S. L. Shang, and Z. K. Liu, *Intermetallics* **18**, 1163 (2010).
- [56] V. E. Osswald, *Zeitschrift Für Phys. A Hadron. Nucl.* **1**, 55 (1933).
- [57] P. Haasen, *Philos. Mag.* **3**, 384 (1958).
- [58] E. N. da C. Andrade and C. Henderson, *Philos. Trans. R. Soc. London A* **244**, 177 (1951).
- [59] D. M. Dimiduk, M. D. Uchic, and T. A. Parthasarathy, *Acta Mater.* **53**, 4065 (2005).
- [60] F. E. Heredia and D. P. Pope, *Acta Metall. Mater.* **39**, 2027 (1991).
- [61] T. Hirano, M. Demura, and D. Golberg, *Acta Mater.* **47**, 3441 (1999).
- [62] W. G. Nöhring and W. A. Curtin, *Acta Mater.* **128**, 135 (2017).
- [63] J. Xiao, H. Cui, H. Zhang, W. Wen, and J. Zhou, *Mater. Sci. Eng. A* 138631 (2019). [In press: DOI: 10.1016/j.msea.2019.138631]
- [64] W. Zhu, D. Fort, I. P. Jones, and R. E. Smallman, *Philos. Mag. Lett.* **77**, 307 (1998).
- [65] T. S. Rong, I. P. Jones, and R. E. Smallman, *J. Phys. IV* **03**, C7 (1993).
- [66] S. Keshavarz and S. Ghosh, *Philos. Mag.* **95**, 2639 (2015).
- [67] Y. Kamimura, K. Edagawa, A. M. Iskandarov, M. Osawa, Y. Umeno, and S. Takeuchi, *Acta Mater.* **148**, 355 (2018).
- [68] K. Edagawa, Y. Kamimura, A. M. Iskandarov, Y. Umeno, and S. Takeuchi, *Materialia* **5**, 100218 (2019).
- [69] Y. Luo, J. Liu, W. Guo, Q. Yu, and S. Li, *J. Dyn. Behav. Mater.* **2**, 223 (2016).

Figures and Figure Captions.

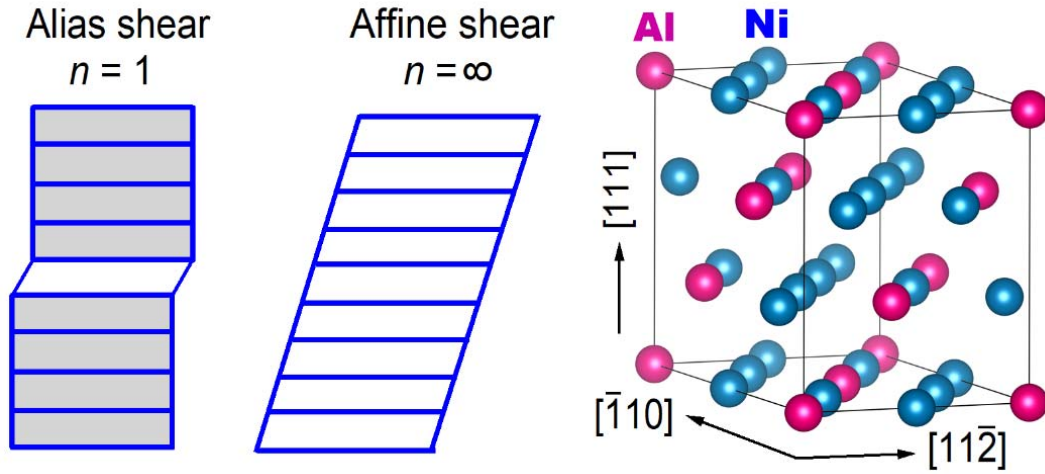


Figure 1. Schematic diagrams of alias shear with atoms in one plane involved during the initial stage of shear (i.e., the number of involved atomic planes $n = 1$, shown as one unshaded area) and affine shear with atoms in all planes involved during the shear ($n = \infty$; all areas are unshaded), together with the 24-atom orthorhombic supercell of Ni_3Al with its lattice vectors parallel to the $[11\bar{2}]$, $[\bar{1}10]$, and $[111]$ directions of the conventional $L1_2$ lattice.

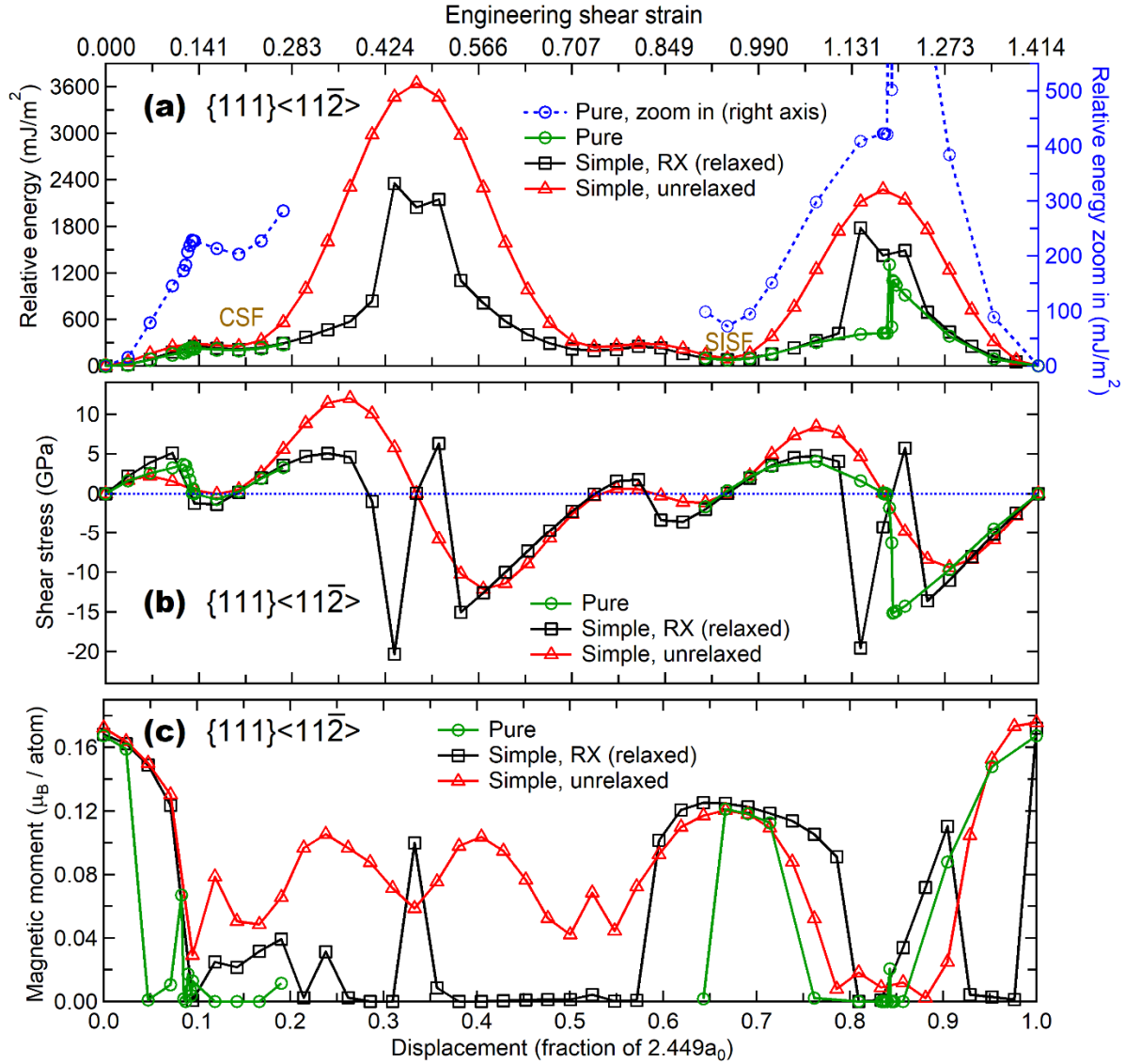


Figure 2. Variations of (a) relative energy, i.e., the γ -surface, (b) shear stress, τ , and (c) magnetic moment of Ni_3Al in terms of $\{111\}\langle 11\bar{2}\rangle$ alias shear using different shear schemes, including pure shear and simple shears with and without relaxations, where a_0 is the lattice parameter of the L_{12} lattice.

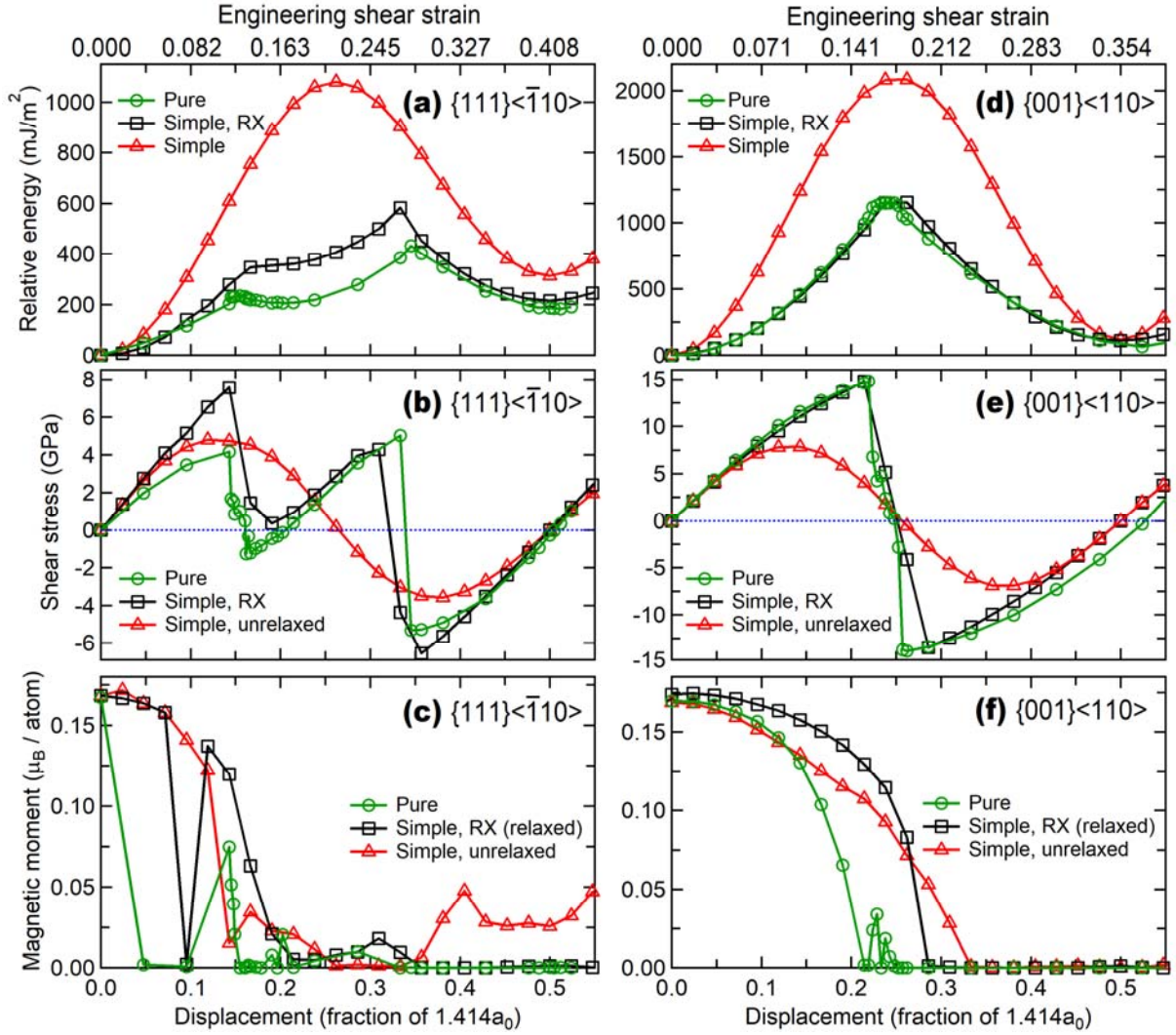


Figure 3. Variations of (a, d) relative energy, i.e., the γ -surface, (b, e) shear stress, τ , and (c, f) magnetic moment of Ni₃Al based on the alias shear deformations of $\{111\}\langle\bar{1}10\rangle$ and $\{001\}\langle 110\rangle$ using different shear schemes, including pure shear and simple shears with and without relaxations, where a_0 is the lattice parameter of L1₂ lattice.

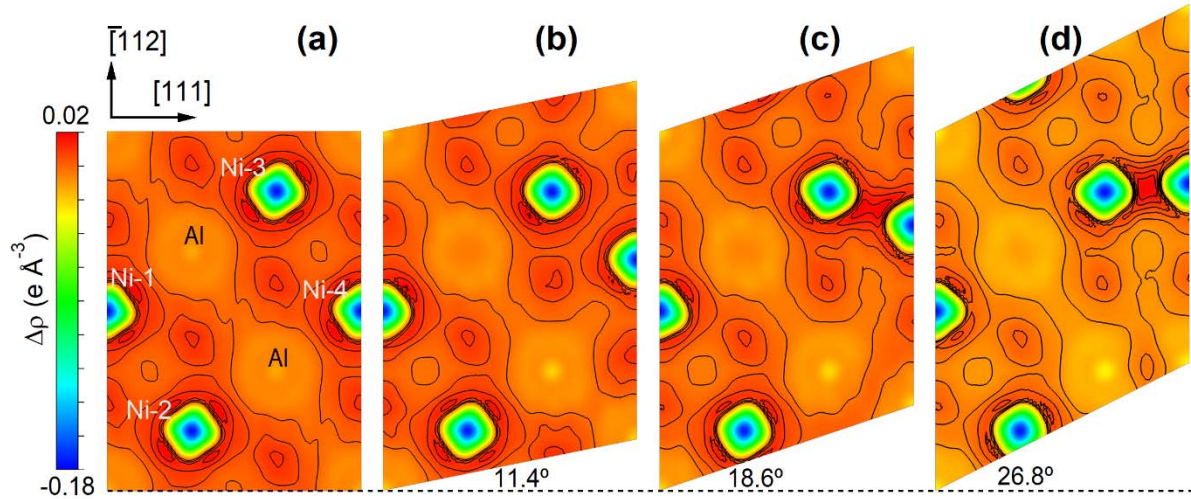


Figure 4. Contour maps of differential charge density ($\Delta\rho$, in unit of $e/\text{\AA}^3$) during the $\{111\}\langle 11\bar{2}\rangle$ simple alias shear of Ni_3Al from the initial configuration (a) to the configuration (d) with the highest shear stress.

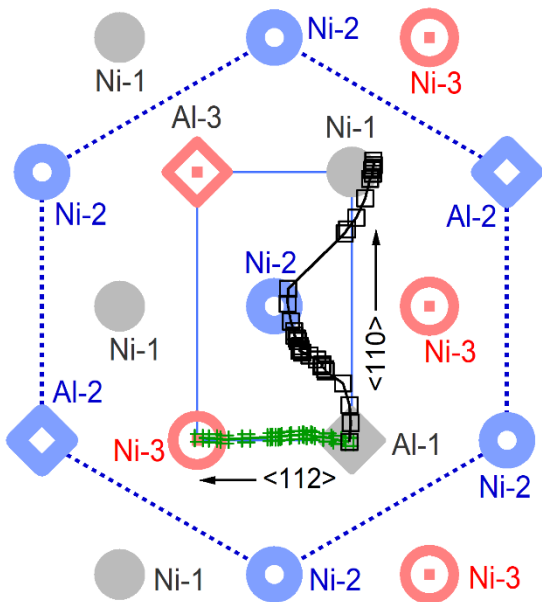


Figure 5. Movement of an Al atom located at the Al-1 position of the $\{111\}$ plane (layer-1) adjacent to the stacking fault plane during the pure alias shear deformations of $\{111\}\langle \bar{1}10\rangle$ (from the Al-1 to Ni-1 position) and $\{111\}\langle 11\bar{2}\rangle$ (from the Al-1 to Ni-3 position). The numbers 1, 2, and 3 indicate three $\{111\}$ layers of Ni_3Al .

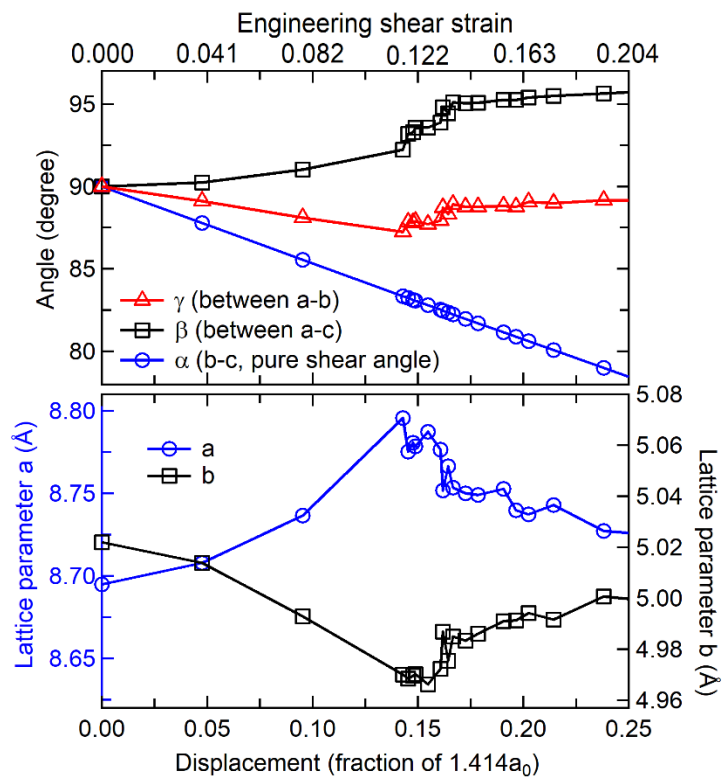


Figure 6. Variations of lattice parameters (a , b , and c) and their angles (α , β , and γ) during the pure alias shear deformation of $\{111\}\langle\bar{1}10\rangle$ for the orthorhombic supercell of Ni_3Al ; see Figure 1.

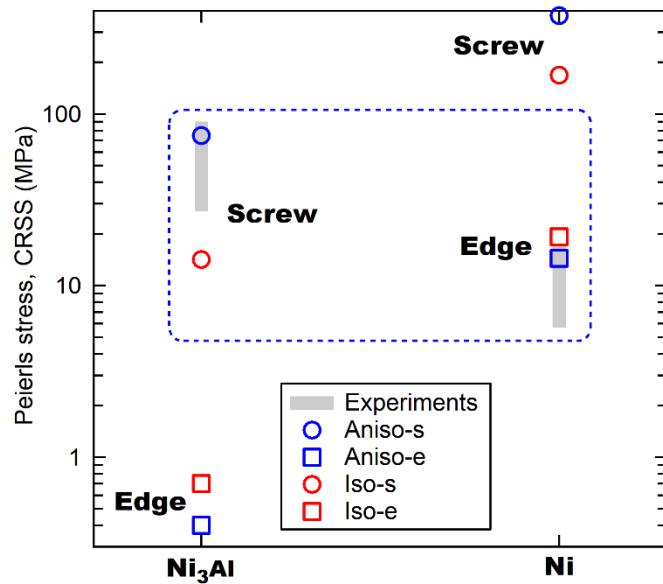


Figure 7. Calculated Peierls stresses at 0 K for four cases of edge (e) and screw (s) dislocations using elastic factors for isotropic (iso) and anisotropic (aniso) crystals in comparison with experimental CRSS values at room temperature for Ni₃Al and Ni; see the detailed values in Table 2.